# Machine Learning-Based Magnetocardiography Model Aids in Diagnosing Non-ST-Segment Elevation Acute Coronary Syndrome in Acute Chest Pain

Junting Li[1–3], Yuheng Zhou[1–3], Ruizhe Wang[1–3], Jiaojiao Pang[3,4], Min Xiang[2,3,5–9], Xiaolin Ning[1]

[1]Beihang University School of Instrumentation and Optoelectronic Engineering, Beijing, China
[2]Key Laboratory of Ultra-Weak Magnetic Field Measurement Technology, Ministry of Education, Beihang University School of Instrumentation and Optoelectronic Engineering, Beijing, China
[3]National Innovation Platform for Industry-Education Integration in Medicine-Engineering Interdisciplinary, Shandong Key Laboratory for Magnetic Field-free Medicine and Functional Imaging, Research Institute of Shandong University, Jinan, China
[4]Department of Emergency Medicine, Shandong Provincial Clinical Research Center for Emergency and Critical Care Medicine, Qilu Hospital of Shandong University, Jinan, China
[5]State Key Laboratory of Traditional Chinese Medicine Syndrome, National Institute of Extremely-weak Magnetic Field Infrastructure, Hangzhou, China
[6]Zhejiang Provincial Key Laboratory of Ultra-Weak Magnetic-Field Space and Applied Technology, Hangzhou, China
[7]Zhejiang Key Laboratory of Zero Magnetic Medicine, Hangzhou, China
[8]Hefei National Laboratory, Hefei, China
[9]Hangzhou Lingci Medical Equipment Co. Ltd, Hangzhou, China

**Background:** Non-ST-segment elevation acute coronary syndrome (NSTE-ACS) is a leading cause of acute chest pain in clinical practice. Magnetocardiography (MCG) is a non-invasive and rapid functional imaging technique with high sensitivity to early, subtle electrophysiological changes associated with myocardial ischemia.

**Aims:** To develop and validate a machine learning (ML)-based diagnostic model for NSTE-ACS using MCG-derived features.

**Study Design:** Retrospective cohort study.

**Methods:** Patients presenting with acute chest pain and admitted between September 2023 and May 2024 were consecutively enrolled. Pretreatment cardiac magnetic signals were collected using a 36-channel optically pumped magnetometer-based MCG system. A total of 13 feature categories (188 parameters) were extracted from the ST segment and T wave. Three feature selection methods [Boruta, least absolute shrinkage and selection operator (LASSO), and maximum relevance minimum redundancy], along with hyperparameter tuning and unbiased performance estimation for five ML algorithms, were implemented within a nested cross-validation (CV) framework. Model performance was assessed using the area under the curve (AUC). The optimal model was further validated in an independent test set. SHapley Additive exPlanations (SHAP) were used to interpret the final model.

**Results:** A total of 578 patients were included (366 with NSTE-ACS and 212 without NSTE-ACS). The support vector machine (SVM) model, based on nine LASSO-selected features, demonstrated the best performance, achieving an AUC of 0.91 ± 0.01 in nested CV. In the independent test set, the model achieved an AUC of 0.89 (95% confidence interval: 0.81–0.95), with an accuracy of 0.84, sensitivity of 0.89, and specificity of 0.77. Exploratory subgroup analyses showed consistent performance across age, sex, body mass index, and comorbidity groups. SHAP analysis identified the minimum magnetic field strength at the T-peak time (T_min_mag) as the most influential predictor.

**Conclusion:** The SVM–based MCG model showed strong potential as an auxiliary tool for identifying NSTE-ACS. Its application may improve chest pain management and reduce misdiagnoses.

**Corresponding author:** Xiaolin Ning, Beihang University, School of Instrumentation and Optoelectronic Engineering, Beijing, China

**e-mail:** ningxiaolin@buaa.edu.cn

**Corresponding author:** Min Xiang, Key Laboratory of Ultra-Weak Magnetic Field Measurement Technology, Ministry of Education, Beihang University School of Instrumentation and Optoelectronic Engineering, Beijing, China

**e-mail:** xiang_min@buaa.edu.cn

**Received:** February 2, 2026 **Accepted:** April 2, 2026 **Available Online Date:** xxxxxx • **DOI:** 10.4274/balkanmedj.galenos.2026.2026-1-319

Available at www.balkanmedicaljournal.org

**ORCID iDs of the authors:** J.L. 0000-0001-6844-4765; Y.Z. 0009-0007-4064-1151; R.W. 0009-0000-7105-0249; J.P. 0009-0002-7781-518X; M.X. 0000-0002-0239-3392; X.N. 0000-0003-3563-3601.

**Cite this article as:** Li J, Zhou Y, Wang R, Pang J, Xiang M, Ning X. Machine Learning-Based Magnetocardiography Model Aids in Diagnosing Non-ST-Segment Elevation Acute Coronary Syndrome in Acute Chest Pain. Balkan Med J. 2026;43:

## INTRODUCTION

As a leading cause of cardiovascular mortality, acute coronary syndrome (ACS) remains a major global public health challenge.[1] Characterized by sudden onset and rapid progression, it often initially presents as acute chest pain.[1] Non-ST-segment elevation ACS (NSTE-ACS), which includes unstable angina (UA) and non-ST-segment elevation myocardial infarction (NSTEMI), accounts for approximately 70% of ACS cases.[2] Currently, initial screening for NSTE-ACS relies on clinical presentation, dynamic electrocardiographic (ECG) changes, and high-sensitivity cardiac troponin (hs-cTn) testing.[2] However, more than 30% of patients with NSTE-ACS do not exhibit typical ST–T changes on ECG, and approximately 15–20% show no significant elevation in hs-cTn levels. These limitations make it difficult to distinguish NSTE-ACS from chest pain caused by other cardiac or non-cardiac conditions, leading to missed or misdiagnoses.[3] These diagnostic challenges increase the risk of adverse outcomes, including recurrent ischemia, heart failure, and long-term cardiovascular events.[4,5] Therefore, there is a need for a sensitive auxiliary tool capable of detecting early myocardial electrophysiological abnormalities.

Magnetocardiography (MCG) is a non-invasive, radiation-free technique that detects weak magnetic fields generated by cardiac electrical activity.[6] Compared with ECG, MCG provides higher spatial resolution and deeper tissue penetration, demonstrates greater sensitivity to tangential currents and subepicardial electrical activity, and is not affected by variations in tissue conductivity.[7-10] These technical advantages make MCG particularly suitable for detecting subtle electrophysiological alterations associated with myocardial ischemia. MCG systems acquire both temporal and spatial information on cardiac magnetic fields and generate multidimensional images with quantitative biomarkers, enabling comprehensive cardiac assessment.[10,11] Previous studies have demonstrated the potential of MCG in diagnosing coronary artery disease, arrhythmias, and other cardiac conditions, offering a novel diagnostic approach.[12] MCG devices primarily employ four types of magnetic sensors, among which the optically pumped magnetometer (OPM) is distinguished by its high sensitivity, compact size, lack of cryogenic cooling requirements, and lower maintenance costs.[11,13] These features enhance its suitability for clinical application. In three studies, a 36-channel OPM-MCG system demonstrated a sensitivity of 67–91% and an area under the curve (AUC) of 0.78–0.86 for detecting myocardial ischemia.[14-16] By extracting early, cardiac-specific MCG biomarkers and developing diagnostic models, MCG has the potential to facilitate earlier detection of cardiovascular diseases.

Machine learning (ML) algorithms can automatically identify patterns in complex datasets and have been widely applied to integrate medical imaging and clinical data for disease prediction.[17] The combination of MCG-derived features with ML approaches may provide reliable clinical decision support. Therefore, this study aimed to develop an intelligent diagnostic model based on MCG features for the rapid and accurate identification of patients with NSTE-ACS.

## MATERIALS AND METHODS

This study was a single-center, retrospective observational cohort study. The protocol was approved by the Qilu Hospital of Shandong University Ethics Committee (approval number: KYLL-202204 (XZ)-017-1; date: 01.09.2023). The study was registered at ClinicalTrials.gov (NCT05392712). Written informed consent was obtained from all participants.

### *Study population*

This study consecutively enrolled patients with suspected NSTE-ACS between September 2023 and May 2024 from the departments of cardiology and emergency medicine. All clinical data were extracted from the electronic medical record system. A total of 933 patients were screened, of whom 355 were excluded based on the predefined inclusion and exclusion criteria.

To ensure the robustness of subsequent analyses, the adequacy of the sample size was evaluated. The study included a consecutive cohort of all eligible patients during a fixed recruitment period, resulting in a final sample of 578 patients. This enrollment strategy minimized selection bias and enhanced the representativeness of the study population. To further assess the adequacy of the sample size for predictive modeling, a post-hoc analysis based on the events-per-variable (EPV) criterion was performed. With 366 NSTE-ACS cases and a final model including nine predictors, the EPV was 40.7 (366/9), which substantially exceeds the recommended minimum threshold of 10–15.

The inclusion criteria were as follows: (1) age ≥ 18 years with a definitive clinical diagnosis; UA was defined as clinical symptoms consistent with accelerating, new-onset, or rest angina in the absence of myocardial necrosis [hs-cTn below the 99th percentile upper reference limit (URL) without dynamic changes], accompanied by transient or dynamic ischemic ECG changes (ST-segment depression ≥ 0.05 mV or T-wave inversion). Confirmation of obstructive coronary artery disease (≥ 50% stenosis) by coronary angiography (CAG) or coronary computed tomography angiography (CCTA) served as supportive evidence of an ischemic origin.[1] NSTEMI was defined as the presence of symptoms of acute myocardial ischemia with a dynamic rise and/or fall in hs-cTn above the 99th percentile URL, without persistent ST-segment elevation on ECG.[1-3] All CCTA images were independently reanalyzed by two senior cardiovascular radiologists blinded to the final clinical diagnosis. In cases where CCTA suggested significant stenosis (≥ 50%) but CAG was not performed, the images were further reviewed by a third expert to reach a consensus, thereby minimizing the risk of misclassification; (2) patients with chest pain initially suspected of NSTE-ACS; and (3) availability of MCG data acquired before treatment. The exclusion criteria were as follows: (1) prior myocardial infarction; (2) complex arrhythmias, congenital heart disease, severe valvular heart disease, hypertrophic or dilated cardiomyopathy; (3) claustrophobia; (4) presence of non-removable metallic implants that could interfere with MCG signals (e.g., cardiac pacemakers, defibrillators, orthopedic implants, or metal dentures); and (5) poor-quality MCG images.

### MCG acquisition and signal preprocessing

MCG data were acquired using a 36-channel OPM-based MCG system with a sampling rate of 1 kHz. The system operates at room temperature without requiring cryogenic cooling, making it suitable for routine clinical use. The sensor array was uniformly arranged in a 6 × 6 grid covering an area of 275 mm × 275 mm and was positioned at a fixed distance of 20 mm from the chest wall to record cardiac electrical activity. For each participant, continuous MCG signals were recorded for 3 minutes. The equipment configuration and sensor placement are illustrated in Figure 1, and the operating procedure was consistent with previously published methods.[18]

Each examination, including patient preparation and signal acquisition, required approximately 5–10 minutes. Real-time waveform visualization was available during recording to ensure data quality. Although sensor positioning relative to cardiac anatomical landmarks is operator-dependent, all recordings were performed by blinded physicians following a standardized protocol. Subsequent signal preprocessing and feature extraction were fully automated using analysis software integrated into the MCG system. This automation minimizes manual intervention and reduces potential operator-related variability.

As shown in Figure 1, the raw MCG signals were evaluated and preprocessed, and subsequently reconstructed into three types of representations: (1) a one-dimensional butterfly map generated by superimposing time-domain waveforms from all 36 channels; (2) a two-dimensional magnetic field map illustrating the spatial distribution of magnetic field intensity at a given time point; and (3) a current density map derived from the magnetic field distribution, representing the spatial distribution of cardiac current density.

### MCG parameters extraction

Based on established clinical knowledge that NSTE-ACS often presents with ST-segment or T-wave abnormalities on ECG, and with reference to previously published studies, we systematically extracted 13 categories of features from the ST segment and T wave, comprising a total of 188 parameters, as candidate predictors. The extracted features included one-dimensional parameters derived from 36 channels (ST_PM, T_amp, ST_level, ST_amp, ST_score, and T_inv); MFM features at the T-peak time (T_max_mag, T_min_mag, T_posi_circ, and T_negi_circ); and CDM features at the T-peak time (T_MCV_pos_x, T_MCV_pos_y, and TT_CMD). The definitions and interpretations of all parameters are summarized in Figure 1.

These MCG parameters are conceptually aligned with conventional ECG findings. Specifically, ST-segment–related parameters (ST_PM, ST_level, ST_amp, and ST_score) reflect ventricular repolarization abnormalities analogous to ST-segment changes on ECG, whereas T-wave–related parameters (T_amp, T_min_mag, T_max_mag, T_posi_circ, and T_negi_circ) correspond to T-wave morphology and repolarization dispersion. This correspondence may facilitate clinical interpretation by cardiologists familiar with standard electrocardiography.

## Model development

### Data splitting

The dataset was stratified by disease status and randomly divided into a training cohort (80%) and an independent test cohort (20%). The test cohort was reserved exclusively for final model evaluation and was not involved in feature selection, hyperparameter optimization, or model development.

Five ML algorithms were developed and internally validated: random forest (RF), logistic regression (LR), support vector machine (SVM), decision tree (DT), and Naive Bayes (NB). To obtain an unbiased estimate of model generalizability, a nested cross-validation (CV) framework was implemented within the training cohort. The outer loop employed a 5-fold stratified CV, generating five training–validation splits. Within each outer fold, an inner 5-fold stratified CV was conducted on the corresponding training subset for feature selection and hyperparameter tuning.

No missing data were identified. Before model development, Z-score normalization was applied to the 188 MCG features to account for differences in scale and measurement units. Standardization parameters [mean and standard deviation (SD) for each feature] were derived exclusively from the training cohort and subsequently applied to the validation folds (within nested CV) and the independent test set to prevent data leakage.

### Feature selection

Within each inner CV fold, three feature selection methods—least absolute shrinkage and selection operator (LASSO), maximum relevance minimum redundancy (mRMR), and the Boruta algorithm—were applied to identify predictive features. To control dimensionality and prioritize informative predictors, features selected in at least 60% of the inner folds were defined as stable, with a maximum of 20 retained. These stable features were subsequently used for model training and evaluated in the corresponding outer validation fold to ensure consistent performance across data subsets.

### Hyperparameter tuning

Grid search was performed within the inner validation folds to identify the optimal hyperparameter combinations for each algorithm, using the AUC as the selection criterion. The following hyperparameters were optimized: max_depth, min_samples_split, n_estimators, and min_samples_leaf for RF; C, penalty, and solver for LR (with max_iter fixed at 2000); C, gamma, and kernel for SVM; and max_depth, min_samples_split, and min_samples_leaf for DT. No hyperparameter tuning was required for the NB algorithm.

### Model development and validation

Using the stable features and optimal hyperparameters identified in each inner CV loop, all ML models were retrained on the corresponding outer training subsets and evaluated on the matched outer validation subsets.

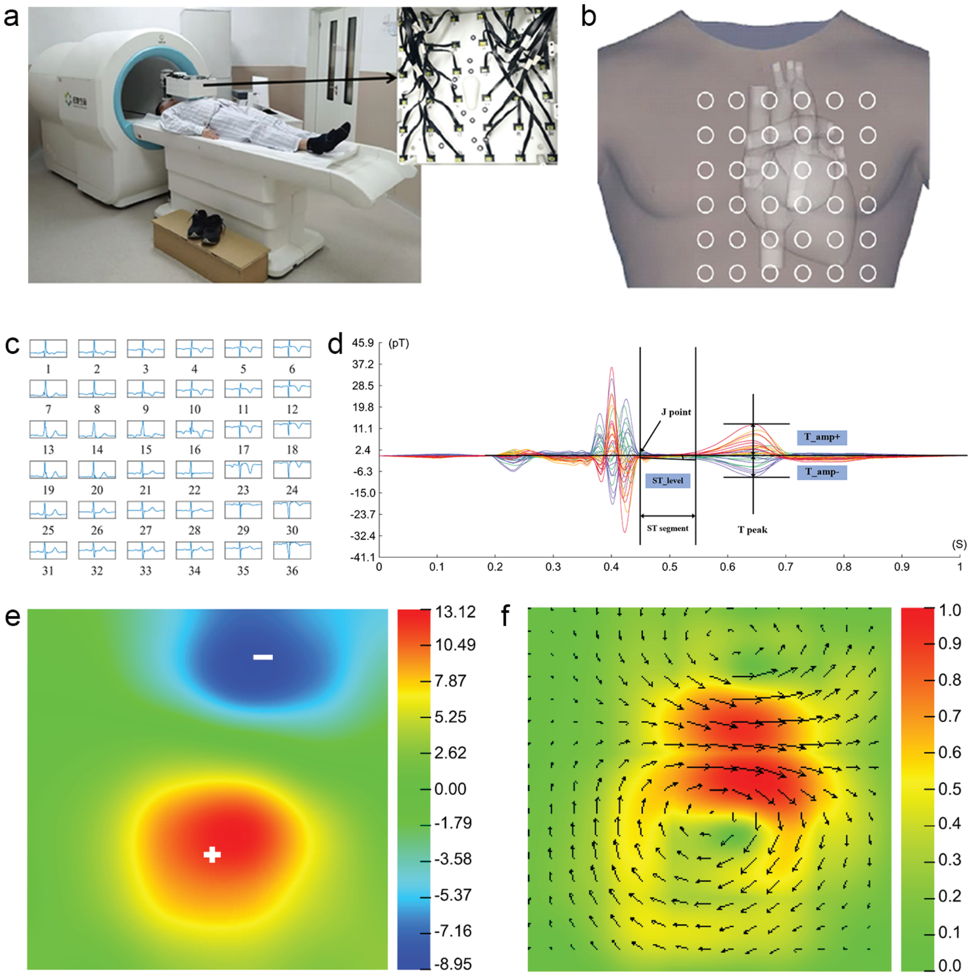

**FIG. 1.** Magnetocardiography (MCG) device, sensor arrangement, and definitions of all MCG parameters. (a) MCG equipment and arrangement of sensors array, (b) relative position of the sensor to the chest, (c) 36-channel MCG waveform, (d) Butterfly diagram. ST_PM: the average magnetic field intensity of the first 100 ms within the ST segment (pT/ms). T_amp: the magnetic field intensity at the T peak time (pT). ST_level: the amplitude of ST segment magnetic field intensity variation (pT). ST_amp: the magnetic field intensity at the ST segment starting point (J point) (pT). ST_score: the total magnetic field intensity changes between the extreme points of the ST segment (pT). T_inv: the consistency of polarity between T wave and R wave. (e) Magnetic field map at the T peak time. The vertical bar on the right indicates magnetic field magnitude; red areas represent positive values; blue areas represent negative values. T_max_mag: maximum magnetic induction intensity at the T peak time (pT). T_min_mag: minimum magnetic induction intensity at the T peak time (pT). T_posi_circ: roundness of the positive area at the T peak time. T_negi_circ: roundness of the negative area at the T peak time. (f) Current density map at the T peak time. T_MCV_pos_x: x-coordinate of the maximum current density at the T peak time. T_MCV_pos_y: y-coordinate of the maximum current density at the T peak time. TT_CMD: maximum instantaneous rate of change of current intensity during T wave period.

This nested CV procedure produced five independent performance estimates per algorithm. Model discrimination was assessed using the AUC, sensitivity, specificity, positive predictive value, negative predictive value, accuracy, and F1 score. These metrics were aggregated as mean ± SD to provide an unbiased estimate of model generalizability.

### Optimal algorithm and final model evaluation

The algorithm with the highest mean AUC and the smallest SD was designated as the optimal model. To develop the final deployable model, the most stable features and the hyperparameter combinations most frequently identified in the inner CV loops were selected. This model was then retrained on the entire training set and evaluated on the independent test set.

The 95% confidence intervals (CIs) for all performance metrics were calculated using 1,000 bootstrap samples to assess result stability. The optimal discrimination threshold was determined by maximizing the Youden index (sensitivity + specificity − 1) in the training set. The performance of the final model was further compared with the thrombolysis in myocardial infarction (TIMI) score, a clinically established risk stratification tool.

Decision curve analysis (DCA) was conducted to evaluate clinical utility, and calibration curves were used to assess agreement between predicted probabilities and observed outcomes. The SHapley Additive exPlanations (SHAP) method quantified and ranked the contribution of each predictor variable to the model's output. A web-based calculator for NSTE-ACS based on the final model was developed and is publicly accessible at https://svm-clinical-calculator-p97ioydfedimtbpfsjdqfp.streamlit.app/.

### Subgroup analysis

Without refitting, exploratory subgroup analyses were performed by applying the final SVM model to predefined subgroups stratified by age (< 57 and ≥ 57 years), sex, body mass index [(BMI); < 25 and ≥ 25 kg/m$^2$], and comorbidities (hypertension, diabetes, and hyperlipidemia). These analyses were descriptive; no statistical comparisons across subgroups or adjustments for multiple testing were performed.

### Statistical analysis

Patient data were summarized as continuous or categorical variables. Continuous variables with a normal distribution were presented as mean ± SD and compared using a t-test, while non-normally distributed variables were reported as median (interquartile range) and analyzed using the Mann–Whitney U test. Categorical variables were expressed as counts and percentages and compared using the chi-square or Fisher's exact test. All statistical analyses and model development were performed using R (version 4.4.3; R Foundation for Statistical Computing, Vienna, Austria) and Python (version 3.13.3). Descriptive analyses were conducted using the R package gtsummary (version 2.2.0). Feature selection was performed using Boruta (Boruta 8.0.0 and randomForest 4.7.1.2), LASSO regression (glmnet 4.1.8), and mRMR (mRMRe 2.1.2.2) in R. The ML pipeline was implemented using Python's scikit-learn library (version 1.8.0), and SHAP analysis was conducted using the shap library (version 0.47.2).

## RESULTS

### Patient characteristics

A total of 578 patients were enrolled, including 366 with NSTE-ACS (286 with UA and 80 with NSTEMI) and 212 non-NSTE-ACS patients. Detailed diagnoses of the non-NSTE-ACS group are presented in Supplementary Table 1. The screening flowchart and study workflow are depicted in Figure 2.

Baseline characteristics and comparisons between groups are summarized in Table 1. The overall mean age was 57.94 ± 11.28 years, 52.9% were male, 46.3% were overweight, and 5.4% were obese. Comorbidities included hypertension (52.6%), type II diabetes (20.1%), and hyperlipidemia (76.0%). Ischemic ECG changes were observed in 54.2% of patients. Compared with the non-NSTE-ACS group, NSTE-ACS patients had a higher proportion of overweight individuals (51.4% vs. 37.7%, $p = 0.002$) and more frequent ischemic ECG changes (62.8% vs. 39.2%, $p < 0.001$). No significant differences were observed in age ($p = 0.194$), sex ($p = 0.153$), or type II diabetes prevalence ($p = 0.659$).

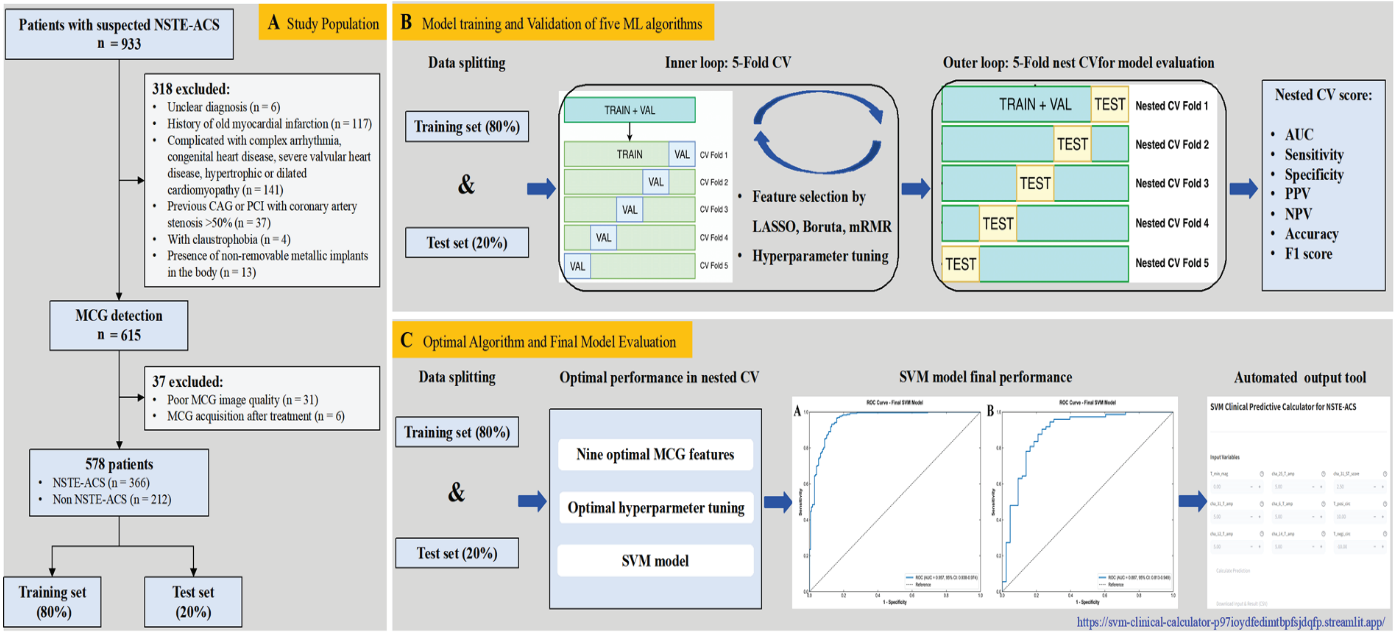

**FIG. 2.** Flowchart of the study. NSTE-ACS, non-ST-segment elevation acute coronary syndrome; CAG, coronary angiography; PCI, percutaneous coronary intervention; MCG, magnetocardiography; CV, cross-validation; LASSO, least absolute shrinkage and selection operator; mRMR, minimum redundancy maximum relevance; AUC, area under the curve; PPV, positive predictive value; NPV, negative predictive value; SVM, support vector machine.

### *Model performance*

Differences in MCG features between groups are detailed in Supplementary Table 2. During nested CV, LASSO and mRMR each selected 9 predictors, while Boruta retained 16 (Supplementary Table 3).

Feature subsets from the three selection methods were separately integrated into five ML algorithms, and model performance was assessed in an unbiased manner. The performance metrics are presented in Table 2. Using the Boruta feature set, SVM achieved an AUC of 0.88 ± 0.01, accuracy of 0.81 ± 0.02, sensitivity of 0.89 ± 0.04,

**TABLE 1.** Patient Characteristics of the Cohort.

| Characteristics | Total (n = 578) | NSTE-ACS (n = 366) | Non-NSTE-ACS (n = 212) | *p* value |
|---|---|---|---|---|
| Age, years | 57.94 ± 11.28 | 57.48 ± 10.02 | 58.75 ± 13.15 | 0.194 |
| Sex (male) | 306 (52.9) | 185 (50.5) | 121 (57.1) | 0.153 |
| BMI (kg/m$^2$) | | | | 0.002 |
| < 18.5 | 9 (1.6) | 2 (0.5) | 7 (3.3) | |
| 18.5 ≤ BMI < 25 | 270 (46.7) | 158 (43.2) | 112 (52.8) | |
| 25 ≤ BMI < 30 | 268 (46.3) | 188 (51.4) | 80 (37.7) | |
| BMI ≥ 30 | 31 (5.4) | 18 (4.9) | 13 (6.1) | |
| Smoke | | | | 0.561 |
| No | 366 (63.3) | 235 (64.2) | 131 (61.8) | |
| Yes | 212 (36.7) | 131 (35.8) | 81 (38.2) | |
| Drink | | | | 0.545 |
| No | 521 (90.1) | 332 (90.7) | 189 (89.2) | |
| Yes | 57 (9.9) | 34 (9.3) | 23 (10.8) | |
| Hypertension | | | | 0.003 |
| No | 274 (47.4) | 191 (52.2) | 83 (39.2) | |
| Yes | 304 (52.6) | 175 (47.8) | 129 (60.8) | |
| Type II diabetes | | | | 0.659 |
| No | 462 (79.9) | 290 (79.2) | 172 (81.1) | |
| Yes | 116 (20.1) | 76 (20.8) | 40 (18.9) | |
| Hyperlipidaemia | | | | 0.012 |
| No | 139 (24.0) | 101 (27.6) | 38 (17.9) | |
| Yes | 439 (76.0) | 265 (72.4) | 174 (82.1) | |
| Ischemic ECG changes | | | | < 0.001 |
| No | 265 (45.8) | 136 (37.2) | 129 (60.8) | |
| Yes | 313 (54.2) | 230 (62.8) | 83 (39.2) | |
| TIMI score | | | | < 0.001 |
| 0 | 114 (19.7) | 37 (10.1) | 77 (36.3) | |
| 1 | 98 (17.0) | 33 (9.0) | 65 (30.7) | |
| 2 | 103 (17.8) | 56 (15.3) | 47 (22.2) | |
| 3 | 127 (22.0) | 108 (29.5) | 19 (9.0) | |
| 4 | 63 (10.9) | 62 (16.9) | 1 (0.5) | |
| 5 | 45 (7.8) | 43 (11.7) | 2 (0.9) | |
| 6 | 17 (2.9) | 16 (4.4) | 1 (0.5) | |
| 7 | 11 (1.9) | 11 (3.0) | 0 (0.0) | |

Values are presented as n (%) or mean ± SD.
BMI, body mass index; ECG, electrocardiographic; NSTE-ACS, non-ST-segment elevation acute coronary syndrome; TIMI, thrombolysis in myocardial infarction; SD, standard deviation.

and specificity of 0.66 ± 0.05, outperforming the other algorithms (AUC range: 0.79–0.87). With the LASSO-selected nine features, SVM and LR achieved the highest AUCs (0.91 ± 0.01 and 0.91 ± 0.03, respectively). Using the mRMR-selected nine features, RF achieved the best performance (AUC: 0.87 ± 0.03; accuracy: 0.83 ± 0.02; F1 score: 0.86 ± 0.02).

To assess generalizability, these three models were retrained on the full training dataset and validated on the independent test set. The SVM model with LASSO-selected features demonstrated superior performance, achieving an AUC of 0.89 (95% CI, 0.81–0.95), accuracy of 0.84 (95% CI, 0.78–0.91), sensitivity of 0.89 (95% CI, 0.81–0.95), specificity of 0.77 (95% CI, 0.63–0.89), and F1 score of 0.88 (95% CI, 0.81–0.93). In comparison, the TIMI score achieved an AUC of 0.82 (95% CI, 0.78–0.85), accuracy of 0.74 (95% CI, 0.71–0.78), sensitivity of 0.66 (95% CI, 0.61–0.71), and specificity of 0.89 (95% CI, 0.85–0.93) (Supplementary Figure 1).

Based on its stability and discriminative ability, the LASSO-based SVM model was selected as the final deployable model. Its receiver operating characteristic (ROC) curves are shown in Figure 3, while the ROC curves for the Boruta-based SVM and mRMR-based RF models are presented in Supplementary Figure 1. The model is publicly accessible as an online calculator at https://svm-clinical-calculator-p97ioydfedimtbpfsjdqfp.streamlit.app/, with source code available at https://github.com/ljting658/svm-clinical-calculator.

### *SVM model explanation*

SHAP analysis quantified the contribution of the nine MCG features to the SVM model's predictions (Figure 4a). T_min_mag (minimum magnetic intensity at the T-wave peak) was the most influential predictor, with a mean SHAP value of 0.12, substantially exceeding all other features and highlighting its discriminative value for NSTE-ACS. The remaining features were ranked in descending order of importance as follows: cha_31_T_amp, cha_12_T_amp, cha_25_T_amp, cha_6_T_amp, cha_14_T_amp, cha_31_ST_score, T_posi_circ, and T_negi_circ.

The SHAP beeswarm plot (Figure 4b) illustrated the positive and negative associations between each feature and NSTE-ACS risk. Increases in T_min_mag, cha_25_T_amp, cha_6_T_amp, T_posi_circ, and T_negi_circ positively influenced predictions, shifting them toward NSTE-ACS. Conversely, increases in cha_31_T_amp, cha_12_T_amp, and cha_14_T_amp negatively influenced predictions, shifting them toward non-NSTE-ACS.

**TABLE 2.** Diagnostic Performance of 5 ML Models and TIMI Score.

| Model | Optimal Threshold | AUC | Sensitivity | Specificity | PPV | NPV | Accuracy | F1 score |
|---|---|---|---|---|---|---|---|---|
| **LASSO** | | | | | | | | |
| **SVM (final model)** | 0.69 | 0.89 (0.81-0.95) | 0.89 (0.81-0.95) | 0.77 (0.63-0.89) | 0.87 (0.78-0.94) | 0.81 (0.68-0.91) | 0.84 (0.78-0.91) | 0.88 (0.81-0.93) |
| SVM | 0.56 ± 0.12 | 0.91 ± 0.01 | 0.90 ± 0.05 | 0.81 ± 0.03 | 0.89 ± 0.01 | 0.83 ± 0.06 | 0.87 ± 0.02 | 0.90 ± 0.02 |
| LR | 0.48 ± 0.21 | 0.91 ± 0.03 | 0.88 ± 0.06 | 0.82 ± 0.04 | 0.90 ± 0.02 | 0.81 ± 0.07 | 0.86 ± 0.03 | 0.89 ± 0.03 |
| RF | 0.55 ± 0.08 | 0.90 ± 0.05 | 0.89 ± 0.07 | 0.77 ± 0.06 | 0.87 ± 0.04 | 0.81 ± 0.11 | 0.85 ± 0.06 | 0.88 ± 0.05 |
| NB | 0.70 ± 0.35 | 0.83 ± 0.04 | 0.89 ± 0.04 | 0.61 ± 0.09 | 0.80 ± 0.03 | 0.77 ± 0.06 | 0.79 ± 0.03 | 0.84 ± 0.02 |
| DT | 0.75 ± 0.10 | 0.82 ± 0.05 | 0.82 ± 0.10 | 0.72 ± 0.06 | 0.83 ± 0.03 | 0.72 ± 0.12 | 0.78 ± 0.06 | 0.82 ± 0.06 |
| **Boruta** | | | | | | | | |
| **SVM (final model)** | 0.46 | 0.85 (0.77-0.92) | 0.91 (0.84-0.96) | 0.70 (0.56-0.84) | 0.84 (0.75-0.90) | 0.82 (0.67-0.93) | 0.83 (0.76-0.89) | 0.87 (0.80-0.92) |
| SVM | 0.56 ± 0.16 | 0.88 ± 0.01 | 0.89 ± 0.04 | 0.66 ± 0.05 | 0.82 ± 0.02 | 0.79 ± 0.06 | 0.81 ± 0.02 | 0.86 ± 0.02 |
| RF | 0.58 ± 0.09 | 0.87 ± 0.02 | 0.87 ± 0.03 | 0.72 ± 0.04 | 0.84 ± 0.02 | 0.76 ± 0.04 | 0.81 ± 0.03 | 0.85 ± 0.02 |
| NB | 0.80 ± 0.40 | 0.86 ± 0.01 | 0.89 ± 0.05 | 0.67 ± 0.06 | 0.83 ± 0.03 | 0.78 ± 0.07 | 0.81 ± 0.03 | 0.85 ± 0.02 |
| LR | 0.55 ± 0.06 | 0.86 ± 0.03 | 0.87 ± 0.04 | 0.73 ± 0.04 | 0.85 ± 0.01 | 0.77 ± 0.05 | 0.82 ± 0.01 | 0.86 ± 0.01 |
| DT | 0.56 ± 0.23 | 0.79 ± 0.02 | 0.79 ± 0.08 | 0.69 ± 0.05 | 0.82 ± 0.02 | 0.66 ± 0.07 | 0.75 ± 0.04 | 0.80 ± 0.04 |
| **mRMR** | | | | | | | | |
| **RF (final model)** | 0.61 | 0.86 (0.78-0.92) | 0.81 (0.71-0.9) | 0.72 (0.59-0.86) | 0.83 (0.74-0.91) | 0.69 (0.55-0.81) | 0.78 (0.7-0.85) | 0.82 (0.75-0.88) |
| RF | 0.54 ± 0.12 | 0.87 ± 0.03 | 0.86 ± 0.07 | 0.76 ± 0.1 | 0.87 ± 0.04 | 0.78 ± 0.08 | 0.83 ± 0.02 | 0.86 ± 0.02 |
| SVM | 0.56 ± 0.18 | 0.85 ± 0.04 | 0.86 ± 0.07 | 0.76 ± 0.09 | 0.86 ± 0.04 | 0.78 ± 0.08 | 0.82 ± 0.03 | 0.86 ± 0.03 |
| NB | 0.91 ± 0.07 | 0.85 ± 0.03 | 0.84 ± 0.02 | 0.74 ± 0.05 | 0.85 ± 0.02 | 0.72 ± 0.03 | 0.8 ± 0.02 | 0.84 ± 0.02 |
| LR | 0.48 ± 0.12 | 0.84 ± 0.04 | 0.85 ± 0.06 | 0.76 ± 0.05 | 0.86 ± 0.02 | 0.75 ± 0.08 | 0.82 ± 0.03 | 0.85 ± 0.03 |
| DT | 0.55 ± 0.28 | 0.79 ± 0.06 | 0.68 ± 0.2 | 0.79 ± 0.09 | 0.85 ± 0.03 | 0.62 ± 0.12 | 0.72 ± 0.1 | 0.73 ± 0.14 |
| **TIMI score** | **3** | **0.82 (0.78-0.85)** | **0.66 (0.61-0.71)** | **0.89 (0.85-0.93)** | **0.91 (0.88-0.95)** | **0.60 (0.55-0.66)** | **0.74 (0.71-0.78)** | **0.76 (0.73-0.80)** |

AUC, area under the curve; PPV, positive predictive value; NPV, negative predictive value; RF, random forest; NB, Naive Bayes; LR, logistic regression; SVM, support vector machine; DT, decision tree; TIMI, thrombolysis in myocardial infarction; ML, machine learning; LASSO, least absolute shrinkage and selection operator; mRMR, maximum relevance minimum redundancy.

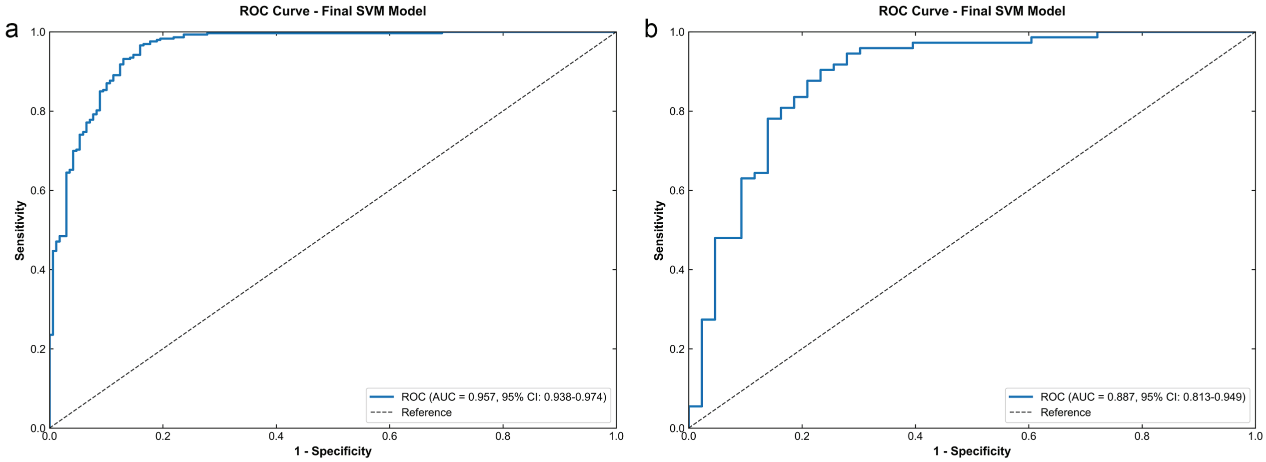

**FIG. 3.** ROC curves of the SVM model. (a) Training set, (b) test set. ROC, receiver operating characteristic; SVM, support vector machine; CI, confidence interval.

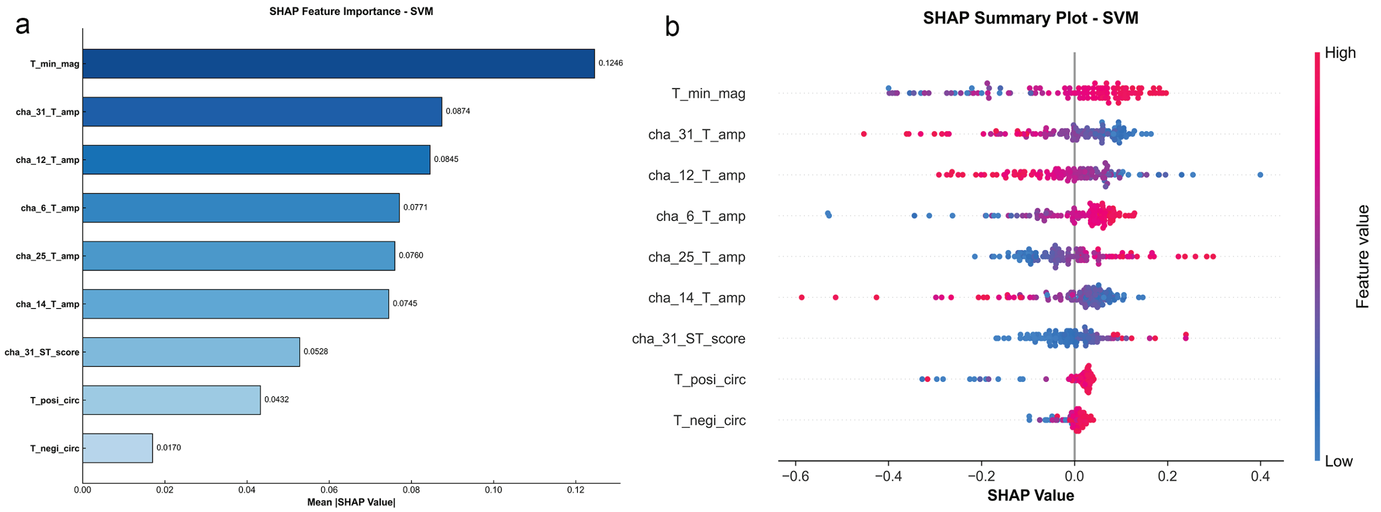

**FIG. 4.** SHAP analysis of feature importance in the SVM model. (a) Feature importance bar plot. Importance was quantified as the mean absolute SHAP value for each feature. (b) SHAP beeswarm plot. The vertical axis is the nine features selected by LASSO, while the horizontal axis is SHAP values, reflecting the contribution of each feature to the model output. Each point represents a subject, with color denoting the feature value (red = high; blue = low). Positive SHAP values shift the prediction toward NSTE-ACS, whereas negative values shift the prediction away from NSTE-ACS. NSTE-ACS, non-ST-segment elevation acute coronary syndrome; SVM, support vector machine; LASSO, least absolute shrinkage and selection operator.

### *DCA and calibration curves of the SVM model*

DCA (Figure 5) demonstrated a positive net benefit for the SVM model across predicted probability thresholds of 0.01–0.89 in the test set and across all thresholds (0.01–0.99) in the training set, indicating its potential clinical utility.

Calibration curves (Figure 6) showed good agreement between predicted probabilities and observed outcomes, with a Brier score of 0.07 in the training set and 0.12 in the test set, indicating favorable and acceptable calibration, respectively.

### *Subgroup analysis of the SVM model*

Exploratory subgroup analyses indicated that the final model maintained high specificity across all subgroups (range: 0.78–0.90) and moderate sensitivity (range: 0.41–0.56) (Supplementary Table 4). Discriminative performance was highest among patients aged < 57 years (AUC: 0.70; 95% CI, 0.63–0.77), BMI < 25 kg/m$^2$ (AUC: 0.71; 95% CI, 0.65–0.78), females (AUC: 0.71; 95% CI, 0.65–0.77), and those with hypertension (AUC: 0.71; 95% CI, 0.65–0.78) or diabetes (AUC: 0.70; 95% CI, 0.65–0.75). Additionally, the model performed better in patients with comorbid diabetes and hyperlipidemia compared with those without these conditions.

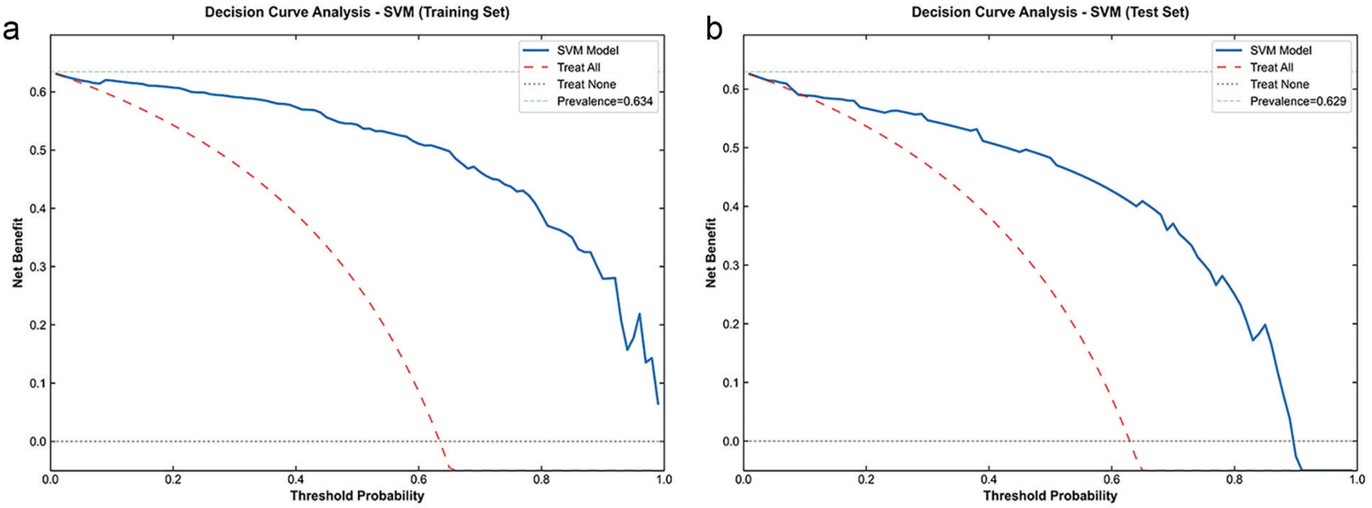

**FIG. 5.** Decision curve analysis for the SVM model in the training and test cohorts. (a) Training cohort, (b) test cohort. SVM, support vector machine.

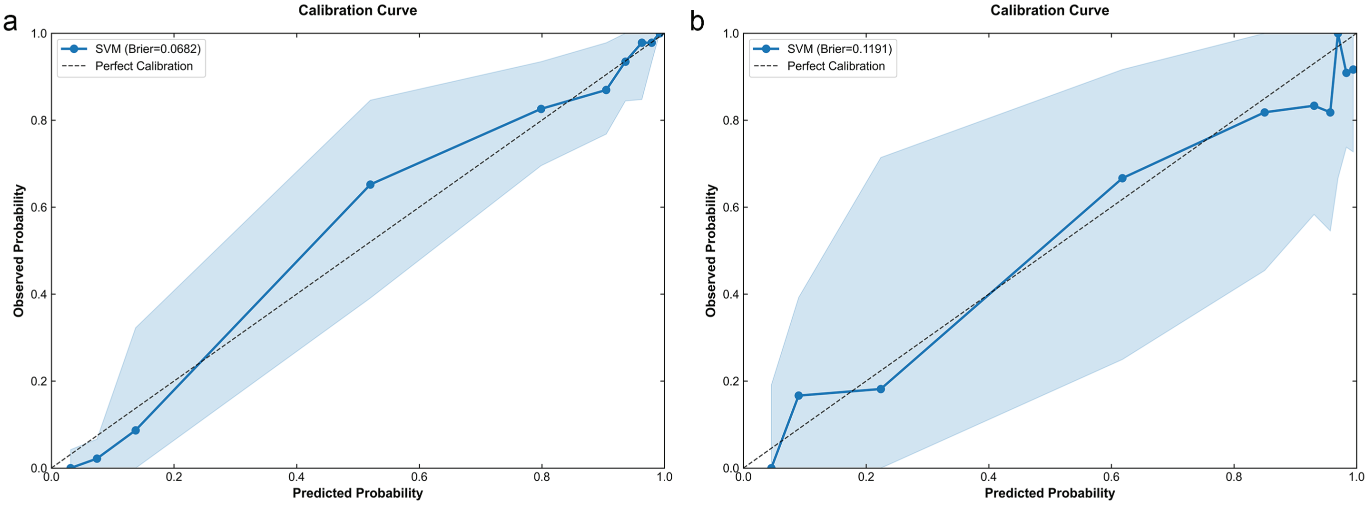

**FIG. 6.** Calibration curves of the SVM model in the training and test cohorts. (a) Training cohort, (b) test cohort. SVM, support vector machine.

## DISCUSSION

This study is the first to develop and validate ML models for diagnosing NSTE-ACS using pretreatment ST-segment and T-wave features derived from MCG. We collected MCG data and clinical information from 578 patients and extracted 13 categories of parameters using a 36-channel OPM-MCG system. The SVM–based diagnostic model achieved the best performance, with an AUC of 0.89 in the independent test set. DCA further confirmed its clinical net benefit and practical utility for early and accurate NSTE-ACS diagnosis.

Existing screening tools show limited sensitivity for NSTE-ACS, with ECG ranging from 30.1% to 44.7%, troponin-I at 42.7%, and echocardiography at 51.0%.[19,20] Specificity is also limited: 85.0–91.1% for ECG, 90.5% for troponin-I, and 76.2% for echocardiography.[19,20] Previous studies have preliminarily explored the diagnostic utility of MCG in coronary artery disease. Zhang et al.[14] developed three models—RF, DT, and SVM—based on MCG parameters from the full cardiac cycle to predict abnormal myocardial perfusion, achieving an AUC of 0.780–0.804. Yang et al.[15] built an LR model using five MCG parameters of the T–T interval to predict myocardial ischemia, reporting an AUC of 0.864 (95% CI 0.803–0.925). Huang et al.[21] used a multilayer perceptron neural network with 10 MCG parameters to construct 11 diagnostic models, with accuracies ranging from 71.2% to 90.5%. Although these studies confirmed the reliability of MCG for diagnosing coronary artery disease, none developed a specific diagnostic model for NSTE-ACS. Only four studies compared MCG parameter differences between patients with NSTEMI or UA and healthy controls, reporting variable diagnostic efficacy with AUCs ranging from 0.56 to 0.93 and accuracies from 0.34 to

0.93.[22-24] These findings highlight the need to clearly define specific MCG parameters for NSTE-ACS.

In this study, we systematically extracted MCG features for NSTE-ACS. Considering the sample size and variable characteristics, we used nested CV for feature selection and hyperparameter tuning and applied five suitable ML algorithms to capture complex non-linear patterns in multidimensional MCG data that elude traditional analytical methods. This approach provided a more robust estimate of model generalizability. The SVM model developed with nine features selected by LASSO performed best, attaining an AUC of 0.91 ± 0.01 in nested CV. In the test set, this model achieved an AUC of 0.89 (95% CI 0.81–0.95), accuracy of 0.84, sensitivity of 0.89, and specificity of 0.77. By comparison, a previous MCG-based study by Lim et al.[23] reported AUCs ranging from 0.62 to 0.87 for distinguishing NSTEMI from healthy controls. Demonstrating stable diagnostic performance comparable to the previously reported AUC of 0.87 for MCG-based coronary artery disease diagnosis.[23] We further compared its performance with the TIMI score, a widely used risk stratification tool for predicting mortality and guiding treatment in NSTE-ACS patients.[25] The SVM model showed superior sensitivity (0.89 vs. 0.66) but lower specificity (0.77 vs. 0.89) than the TIMI score. This complementary profile reflects the TIMI score's prognostic emphasis on specificity, whereas the MCG model captures early electrophysiological abnormalities that enhance detection of subtle ischemia, making it more appropriate for use as a rule-out tool in the acute setting.

Among the 188 MCG parameters extracted, nine were retained in the final SVM model after LASSO-based selection. T_min_mag emerged as the most powerful discriminative indicator, with higher values positively correlated with increased NSTE-ACS risk. This finding underscores the key role of spatial heterogeneity in the magnetic field during ventricular repolarization in identifying NSTE-ACS. T_min_mag may reflect acute ischemia–induced shortening of action potential duration and increased repolarization dispersion, generating local currents that attenuate the ventricular repolarization vector, which manifests as reduced negative magnetic field intensity at the T-wave peak. These results are consistent with previous MCG reports describing increased complexity of magnetic field distribution and decreased extreme-value amplitudes during repolarization in ischemic hearts.[23,24,26,27] Lim et al.[23] reported that patients with NSTEMI exhibited the greatest difference in magnetic field angle at the T-wave peak compared with healthy controls, achieving an AUC of 0.87. Our results further emphasize the significance of MFM parameters.

Exploratory subgroup analyses provided additional insights into the clinical applicability of the SVM model. When applied without refitting, the model consistently demonstrated high specificity across all predefined subgroups, suggesting stable rule-out performance for non-NSTE-ACS patients regardless of age, sex, BMI, or comorbidities. In contrast, sensitivity remained moderate across subgroups, indicating that a negative prediction alone may not definitively exclude NSTE-ACS, particularly in high-risk populations. These findings highlight the potential of the model as an adjunctive screening tool: its high specificity could reduce unnecessary invasive testing in low-risk patients, while its moderate sensitivity supports integration with established clinical assessments when positive. Given the exploratory nature of these analyses and the absence of statistical comparisons across subgroups, these observations should be interpreted cautiously and require validation in larger prospective studies.

This study has several limitations. First, it is a single-center study with a relatively small sample size and lacks external validation, necessitating further confirmation through multicenter studies. Second, variations in the MCG device may affect model performance. Although a 36-channel OPM-MCG system was used, signal preprocessing and parameter extraction relied on specific analytical pipelines, and operational procedures and extraction methods have not yet been standardized, potentially affecting consistency across centers. Third, the single-center design and high comorbidity burden may limit the applicability of our findings to clinical settings with different patient populations. Future multicenter studies incorporating diverse populations with varying risk profiles are warranted to evaluate model robustness and performance across subgroups. Additionally, calibration tailored to specific patient subgroups may enhance clinical applicability in heterogeneous populations. Fourth, although SHAP analysis enhanced model interpretability, quantitative MCG parameters have yet to be standardized, and their underlying pathophysiological mechanisms require further investigation. Fifth, both CCTA and invasive CAG were used as reference standards for confirming obstructive coronary artery disease. Although CCTA images were rigorously reviewed by experienced radiologists to minimize misclassification, inherent differences in diagnostic accuracy between modalities may introduce potential bias. Finally, this study relied solely on MCG parameters and did not integrate multimodal information such as ECG or biomarkers. Future efforts should focus on optimizing feature selection, exploring subgroup-specific thresholds, and developing diagnostic models that integrate multidimensional clinical data to improve specificity and reduce unnecessary interventions.

MCG technology remains in the experimental and exploratory phase and has not yet been adopted as a standardized diagnostic tool in routine clinical practice. Relevant technical specifications, operational protocols, and diagnostic criteria are still under development. Its clinical efficacy and safety require further validation through large-scale, prospective studies. Future research should involve multicenter, long-term follow-up investigations to systematically assess usability and clinical utility in real-world settings.

**Ethics Committee Approval:** The protocol was approved by the Qilu Hospital of Shandong University Ethics Committee (approval number: KYLL-202204 (XZ)-017-1; date: 01.09.2023).

**Informed Consent:** Written informed consent was obtained from all participants.

**Data Sharing Statement:** The data that support the findings of this study are available from the corresponding author upon reasonable request.

**Authorship Contributions:** Concept- J.L., X.N.; Design- J.L., Supervision-J.P., M.X., X.N.; Funding- M.X.; Materials- J.L., Y.Z.; Data Collection or Processing- J.L., Y.Z., R.W.; Analysis and/or Interpretation- J.L., Y.Z.; Literature Review- J.L.; Writing- J.L.; Critical Review- R.W., J.P., M.X.

**Conflict of Interest:** The authors declare that they have no conflict of interest.

**Funding:** This project was supported by the Fundamental and Interdisciplinary Disciplines Breakthrough Plan of the Ministry of Education of China (JYB2025XDXM606), Innovation Program for Quantum Science and Technology (2021ZD0300503), National Natural Science Foundation of China (U23A20485), and Fundamental Research Funds for the Central Universities.

**Supplementary Tables:** https://balkanmedicaljournal.org/img/files/BalkanMedJ-2026-1-319-supple-tables.pdf

**Supplementary Figure:** https://balkanmedicaljournal.org/img/files/2026-1-319-suplement-figure.pdf

## REFERENCES

1. Rao SV, O'Donoghue ML, Ruel M, et al. 2025 ACC/AHA/ACEP/NAEMSP/SCAI guideline for the management of patients with acute coronary syndromes: a report of the American College of Cardiology/American Heart Association Joint Committee on clinical practice guidelines. *Circulation*. 2025;151:e771-e862. [CrossRef]
2. Chinese Society of Cardiology, Chinese Medical Association; Editorial Board of Chinese Journal of Cardiology. [Guidelines for the management of non-ST elevation acute coronary syndromes (2024)]. *Zhonghua Xin Xue Guan Bing Za Zhi*. 2024;52:615-646. [CrossRef]
3. Thygesen K, Alpert JS, Jaffe AS, et al. Fourth universal definition of myocardial infarction (2018). *Circulation*. 2018;138:e618-e651. [CrossRef]
4. Balasubramanian RN, Mills GB, Wilkinson C, Mehran R, Kunadian V. Role and relevance of risk stratification models in the modern-day management of non-ST elevation acute coronary syndromes. *Heart*. 2023;109:504-510. [CrossRef]
5. Kovacevic M, Jones DA, Thiele H, Steg PG, Kunadian V. Diagnosis, risk stratification, and early management of non-ST-segment elevation acute coronary syndrome. *EuroIntervention*. 2025;21:e1399-e1423. [CrossRef]
6. Wang Y, Zhao ZG, Chai Z, Fang JC, Chen M. Electromagnetic field and cardiovascular diseases: a state-of-the-art review of diagnostic, therapeutic, and predictive values. *FASEB J*. 2023;37:e23142. [CrossRef]
7. Plonsey R. Capability and limitations of electrocardiography and magnetocardiography. *IEEE Trans Biomed Eng*. 1972;19:239-244. [CrossRef]
8. Gapelyuk A, Wessel N, Fischer R, et al. Detection of patients with coronary artery disease using cardiac magnetic field mapping at rest. *J Electrocardiol*. 2007;40:401-407. [CrossRef]
9. Smith FE, Langley P, van Leeuwen P, et al. Comparison of magnetocardiography and electrocardiography: a study of automatic measurement of dispersion of ventricular repolarization. *Europace*. 2006;8:887-893. [CrossRef]
10. Dutz S, Bellemann ME, Leder U, Haueisen J. Passive vortex currents in magneto- and electrocardiography: comparison of magnetic and electric signal strengths. *Phys Med Biol*. 2006;51:145-151. [CrossRef]
11. Han X, Pang J, Xu D, et al. Coronary artery disease severity and location detection using deep-mining-based magnetocardiography pattern features. *Comput Methods Programs Biomed*. 2025;266:108764. [CrossRef]
12. Li J, Shen Y, Shen C, Ning X, Xiang M. Advances of magnetocardiography in application of adult and fetal cardiac diseases. *Front Cardiovasc Med*. 2025;12:1522467. [CrossRef]
13. Strand S, Lutter W, Strasburger JF, Shah V, Baffa O, Wakai RT. Low-cost fetal magnetocardiography: a comparison of superconducting quantum interference device and optically pumped magnetometers. *J Am Heart Assoc*. 2019;8:e013436. [CrossRef]
14. Zhang H, Ma Z, Mi H, et al. Diagnostic value of magnetocardiography to detect abnormal myocardial perfusion: a pilot study. *Rev Cardiovasc Med*. 2024;25:379. [CrossRef]
15. Yang S, Feng L, Zhang M, et al. Development and validation of a clinical diagnostic model for myocardial ischaemia in borderline coronary lesions based on optical pumped magnetometer magnetocardiography: a prospective observational cohort study. *BMJ Open*. 2024;14:e086433. [CrossRef]
16. Mace SE, Peacock WF, Stopyra J, et al. Accelerated magnetocardiography in the evaluation of patients with suspected cardiac ischemia: The MAGNETO trial. *Am Heart J Plus*. 2024;40:100372. [CrossRef]
17. Haug CJ, Drazen JM. Artificial intelligence and machine learning in clinical medicine, 2023. *N Engl J Med*. 2023;388:1201-1208. [CrossRef]
18. Wu T, Zhao X, Feng L, et al. Comparison of magnetocardiography and coronary computed tomographic angiography for detection of coronary artery stenosis and the influence of calcium. *Eur Radiol*. 2025;35:4775-4785. [CrossRef]
19. Kwon H, Kim K, Lee YH, et al. Non-invasive magnetocardiography for the early diagnosis of coronary artery disease in patients presenting with acute chest pain. *Circ J*. 2010;74:1424-1430. [CrossRef]
20. Park JW, Hill PM, Chung N, Hugenholtz PG, Jung F. Magnetocardiography predicts coronary artery disease in patients with acute chest pain. *Ann Noninvasive Electrocardiol*. 2005;10:312-323. [CrossRef]
21. Huang X, Chen P, Tang F, Hua N. Detection of coronary artery disease in patients with chest pain: a machine learning model based on magnetocardiography parameters. *Clin Hemorheol Microcirc*. 2021;78:227-236. https://doi.org/10.3233/CH-200905
22. Goodacre S, Walters SJ, Qayyum H, et al. Diagnostic accuracy of the magnetocardiograph for patients with suspected acute coronary syndrome. *Emerg Med J*. 2021;38:47-52. [CrossRef]
23. Lim HK, Chung N, Kim K, et al. Can magnetocardiography detect patients with non-ST-segment elevation myocardial infarction? *Ann Med*. 2007;39:617-627. [CrossRef]
24. Lim HK, Kwon H, Chung N, et al. Usefulness of magnetocardiogram to detect unstable angina pectoris and non-ST elevation myocardial infarction. *Am J Cardiol*. 2009;103:448-454. [CrossRef]
25. Antman EM, Cohen M, Bernink PJ, et al. The TIMI risk score for unstable angina/non-ST elevation MI: a method for prognostication and therapeutic decision making. *JAMA*. 2000;284:835-842. [CrossRef]
26. Zhao C, Jiang S, Wu Y, et al. An integrated maximum current density approach for noninvasive detection of myocardial infarction. *IEEE J Biomed Health Inform*. 2018;22:495-502. [CrossRef]
27. Kyoon Lim H, Kim K, Lee YH, Chung N. Detection of non-ST-elevation myocardial infarction using magnetocardiogram: new information from spatiotemporal electrical activation map. *Ann Med*. 2009;41:533-546. [CrossRef]